Spin/valley polarization in bulk MoS_2

R. Suzuki,[1*] M. Sakano,[1*] Y. J. Zhang,[1] R. Akashi,[1] D. Morikawa,[2] A. Harasawa,[3] K. Yaji[3], K. Kuroda[4], K. Miyamoto[5], T. Okuda[5], K. Ishizaka,[1¶] R. Arita,[1,2] and Y. Iwasa[1, 2¶]

[1]Quantum-Phase Electronics Centre (QPEC) and Department of Applied Physics, University of Tokyo, Tokyo 113-8656, Japan

[2]RIKEN Centre for Emergent Matter Science, Wako 351-0198, Japan

[3] Institute for Solid State Physics, University of Tokyo, Kashiwa, 277-8581, Japan

[4]Graduate School of Science, Hiroshima University, Higashi-Hiroshima 739-8526, Japan

[5]Hiroshima Synchrotron Radiation Centre, Hiroshima University, Higashi-Hiroshima 739-0046, Japan

The valley degree of freedom of electrons is attracting growing interests as a carrier of information in various materials including graphene, diamond and monolayer transition metal dichalcogenides. The latter are semiconducting and are unique due to the coupling between spin and valley, originating from the relativistic spin-orbit interaction. Here we report a direct observation of valley-dependent out-of-plane spin polarization in an archetypal transition metal dichalcogenide, MoS_2 by means of spin- and angle-resolved photoemission spectroscopy. The result was in fair agreement with first principles theoretical prediction. This became possible by choosing a 3R polytype crystal which has a noncentrosymmetric structure, in contrast to the conventional centrosymmetric 2H form. Furthermore, we confirmed robust valley polarization in the 3R form by means of circular polarized photoluminescence spectroscopy. Noncentrosymmetric transition metal dichalcogenide crystals may provide a firm basis for the development of magnetic and electric manipulation of spin/valley degrees of freedom.

---

[*] These authors contributed equally to this work.

¶Corresponding author: iwasa@ap.t.u-tokyo.ac.jp and ishizaka@ap.t.u-tokyo.ac.jp

Transition Metal Dichalcogenides (TMDC) based two dimensional (2D) atomic crystals are emerging materials with rich physical properties, such as excellent field effect transistor (FET) performance with a large on-off ratio[1] and an ambipolar mode[2-4], electric field induced superconductivity[5,6] and Zeeman splitting[7], as well as strong photoluminescence (PL)[8-13]. In particular, circular dichroic photoluminescence offers a new opportunity for optoelectronic functionality called valleytronics, i.e. manipulation of the valley degree of freedom as an information carrier. Candidate materials for this direction include silicon[14], diamond[15], AlAs[16-18], bismuth[19], graphene[20-23], and TMDCs[24,25]. Control and detection of valley polarization was indeed demonstrated by optical pumping of monolayer MoS_2 and other TMDCs through PL circular dichroism, taking advantage of the finite band gap, which is absent in graphene[10-13,26,27]. This functionality came from the noncentrosymmetric nature in the monolayer MoS_2, causing finite Berry curvature[24]. As shown in Fig. 1a, the monolayer is formed by covalently bonded S-Mo-S quasi-2D networks with a trigonal structure without inversion symmetry, which is also seen in the side view in Fig. 1b. In the bulk, such 2D monolayers are packed by weak van der Waals forces. The most common bulk phase of MoS_2 is a so called 2H-polytype[28], whose unit cell is composed of a bilayer with the space group of $P6_3/mmc$, having a hexagonal Brillouin Zone and the inversion symmetry is restored in the bulk crystal (Figs. 1b,c)[28,29]. The factor which makes TMDC unique is the strong spin-orbit interaction (SOI) due to the *d* orbitals of the heavy metals, which leads to coupled spin/valley physics[24]. For instance, theoretical predictions suggest that the top most valence bands located at the corners (*K*- and *K'*- points) of the 2D hexagonal Brillouin zone undergo a valley-contrasting spin splitting with a polarization perpendicular to the 2D plane[30].

Because of the absence of inversion symmetry, monolayer MoS_2 and other TMDCs are the most suitable materials for spin/valley physics and its application to electronic and optoelectronic devices. Hence, preparation of monolayer systems is the key technology to be developed, and significant amount of efforts have been devoted for fabrication and characterization of monolayer

materials and devices. The major routes to monolayers are the mechanical exfoliation of single crystals[8-13] and chemical vapour deposition[31-33], which usually yield crystalline monolayers with 30 μm at maximum in lateral size. This is large enough for basic electrical transport and optical experiments with micro devices, but not sufficient for deepening spin/valley physics and extending functionalities. For instance, the spin polarization predicted by the theory still remains to be detected. However, the noncentrosymmetric structure should not be limited to monolayer. Recently symmetry control of bilayer or even bulk crystals has been proposed using the FET configurations[7,26,27]. Application of the electric field perpendicular to the bilayer or multilayers makes the each layer inequivalent, and consequently, the in-plane inversion asymmetry is restored. Such manipulation of crystal symmetry by external field is vital for controlling the electronic Bloch states at the surface state within the screening length, offering a novel route to mimic the monolayer state.

Here we report a totally different way of controlling the symmetry by taking advantage of the rich polytypism in TMDCs layered materials systems. For the case of MoS_2, in addition to the most stable 2H phase, so called 3R phase having a stacking pattern and the first Brillouin Zone, shown in Figs. 1b,c, respectively, is known to exist as another stable phase[28,29,34]. The space group of the 3R structure is *R3m*, and its unit cell is composed of a trilayer stacked in such a way that the inversion symmetry is kept broken in the bulk form. Using single crystals of the 3R-phase, we successfully observed the out-of-plane spin polarization in the valence band at the $\overline{K}$- and $\overline{K}'$ -points, which displays fair agreement with the first principles band calculations taking the SOI into account. This is the proof of the valley dependent spin polarization expected in the monolayer MoS_2, by use of the multi-layer crystal with noncentrosymmetric stacking pattern of layers. Furthermore, we demonstrate that information of valley polarization in the 3R-stacking is effectively preserved by means of the layer number dependence of PL circular dichroism.

Crystal growth and characterization.

We have grown the 2H- and 3R-MoS_2 with a chemical vapour transport technique, using I_2 and Cl_2 as carrier gases, respectively[29]. Grown crystals were characterized by various methods. First, the powder diffraction pattern clearly demonstrated the difference in crystal symmetry, despite almost identical lattice parameters. Fig. 2a displays optical micrographs of typical surfaces of 2H and 3R single crystals. The screw dislocations observed in these two forms of crystals have hexagonal and trigonal structures, respectively, clearly reflecting their crystal symmetries[35]. Fig. 2b shows convergent-beam electron diffraction (CBED) patterns of 2H-MoS_2 and 3R-MoS_2 with [0001] incidence at room temperature. The patterns unambiguously show the complete pattern symmetries of 6*mm* and 3*m*, respectively, which are consistent with the reported space groups[28]. All these structural characterizations confirmed that 3R phase is dominant when grown with a Cl_2 carrier gas. Optical reflection spectra on the 2H- and 3R-phase are shown in Fig. 2c, in which we observe a twin peak structure at 1.8 – 2.0 eV both in 2H- and 3R-phases. These two peaks are well known excitons associated with the direct optical transitions at the *K*- or *K'*-points in the Brillouin zone. Interestingly, the splitting in the 3R-phase of 0.14 eV is smaller than 0.18 eV in the 2H-phase. This difference in the splitting is another fingerprint to distinguish the two phases, as has been already reported in the transmission spectra in 2H- and 3R-MoS_2[28,36].

Spin- and Angle-Resolved Photoemission Spectroscopy.

For detecting the spin polarization, we started with comparisons of the whole valence band structures determined by angle resolved photoemission spectroscopy (ARPES) and first principles band calculations including the SOI. Figs. 3a,b display the valence band structures of a 3R-MoS_2 bulk crystal obtained by ARPES and calculation. The same comparison is given in Figs. 3c,d for a 2H-MoS_2 bulk crystal whose overall electronic structure is in agreement with previous reports.[37,38] Since both samples are of n-type, the Fermi level (E_F) is fixed near the conduction band bottoms. Considering that the ARPES images for $h\nu$ = 40.8 eV (left) and 21.2 eV (right) both include the

projection of finite k_z-dispersions, they are in good agreement with the calculations. Here $h\nu$ and k_z denote photon energy of the incident light, and the momentum component along the Γ-*A* direction (Fig. 1c). The overall band structures of 3R- and 2H- MoS_2 are found to be very similar reflecting the van der Waals stacking nature of TMDCs. By closely looking into the detailed band structures, nevertheless, small but contrasting differences between 3R and 2H can be noticed. One difference is found at the top of valence band at the $\overline{K}$-point marked by the green rectangles in Figs. 3a,c, which are expanded in Figs. 3e-h. The ARPES data (Figs. 3e,g) indicate that the energy splitting of the valence band top at the $\overline{K}$-point is smaller for 3R compared to 2H-MoS_2 crystal. The values of splitting, approximately 0.14 and 0.17 eV respectively, agree well with those calculated in Figs. 3f, h, though there remains some ambiguity arising from the k_z-dependent dispersion. This agreement becomes more impressive when we compared to Fig. 2c, where we saw the similar difference of the exciton splitting for 3R and 2H crystals. These indicate that the 3R and 2H single crystals can be successfully distinguished from the viewpoint of the electronic structures.

Based on these results, we proceeded to spin and angle resolved photoemission spectroscopy (SARPES), which had been useful for directly detecting the *k*-dependent spin polarizations in a noncentrosymmetric compound[39]. By utilizing three-dimensional spin polarimeter[40,41], spin polarizations along x, y, z directions (P_x, P_y, P_z) can be unambiguously measured. Fig. 4a shows the equi-energy band surfaces of 3R-MoS_2 at $E-E_{\overline{K}}=-0.3$ eV, where $E-E_{\overline{K}}$ represents the energy level relative to the valence band maximum at $\overline{K}$ point. The experimentally obtained images indicate the existence of hole-like equi-energy surfaces around $\overline{\Gamma}$-, $\overline{K}$-, and $\overline{K}'$-points, showing an excellent agreement with the calculated curves. As the spin-resolved calculation indicates by red (spin-up) and blue (spin-down) curves in Fig. 4g, the valence band top at $\overline{K}$-point is expected to show large SOI-induced Zeeman-type band splitting with inverted spin polarization at $\overline{K}'$-point ($P_z \approx \pm 1$). In fact, this was confirmed in the SARPES

spectra, as shown in Fig. 4b. The red (blue) curves indicate the intensity of spin-up (-down) components obtained at $\overline{K}$-point. The spectra for z-oriented spin $<s_z>$ clearly show that the upper (lower) band at the $\overline{K}$-point top is spin-up (-down) polarized, whereas the in-plane $<s_x>$ and $<s_y>$ components have the nearly equivalent intensities. Fig. 4c indeed shows the almost full polarization along *z*-direction ($P_z \sim \pm 1$), in contrast to the very small in-plane P_x, P_y (see SI for detailed analysis). Furthermore, the SARPES $< s_z >$ spectra for $\overline{K}$- and $\overline{K}'$-points as shown in Fig. 4d clearly indicate the inversion of the spin-polarization for both upper and lower bands. It thus offers direct evidence of the valley/spin coupled state realized in bulk 3R-MoS_2, a counterpart of the recently reported Tl/Si(111) surface state.[42] In marked contrast, the valence band tops at $\overline{K}$-point for 2H-MoS_2 and 2H-WSe_2 are much less polarized with negligible inequivalency of spin-up and -down components (Fig. 4e, see SI for the details of SARPES condition), as theoretically expected (Fig. 4h). It suggests that the effect of inversion symmetry breaking at the surface can be ruled out as the origin of the huge spin splitting emerging in the 3R system. To demonstrate the spin-dependent valence band dispersion of 3R-MoS_2, the difference of $<s_z>$ spin-up and -down SARPES intensities are shown in Fig. 4f. This provides a firm and clear image of the out-of-plane spin polarization at the valence band top of the $\overline{K}$-point, in agreement with the calculation in Fig. 4g.

Circular dichroic photoluminescence.

To confirm the valley polarization in the 3R-stacking, we have carried out a PL circular dichroism experiment. We compared circular dichroism on mono- and multi-layers of 3R- and 2H-stackings. For thickness estimation of micro-mechanically cleaved MoS_2 samples, we performed micro Raman spectroscopy experiments, in particular focused on the frequency difference between E^1_{2g} and A_{1g} modes, and atomic force microscope (AFM). For the 2H-stacking, an empirical correlation is established between the energy splitting of the E^1_{2g} and A_{1g} splitting and the number of layers determined by the AFM[43,44]. We found a similar relation holds for the case of the 3R-stacking

even quantitatively, as shown in Supplementary Information Section 4. This allowed us to perform experiments of layer number dependence of PL circular dichroism on 2H- and 3R-MoS_2.

Figure 5a shows the circularly polarized PL spectra of mono- and multi-layers of 3R- and 2H-MoS_2 recorded at 4 K with the σ_- excitation of 633 nm (1.96 eV), where σ_+ (σ_-) denotes right (left) circularly polarized light. All the spectra are composed of sharp Raman and broad PL peaks, the latter of which show a peculiar layer number dependence of circular polarization. For the 2H-stacking, the intensity difference between σ_+ and σ_- PL spectra becomes smaller with increasing the layer numbers, whereas that for the 3R-stacking does not show clear layer number dependences. The degree of circular dichroic polarization ρ defined as $\frac{I(\sigma_-) - I(\sigma_+)}{I(\sigma_-) + I(\sigma_+)}$ under the σ_- excitation is plotted against the layer number N in Fig. 5b both for the 3R- and 2H-multilayers. Here $I(\sigma_+)$ and $I(\sigma_-)$ denote the PL intensity of σ_+ and σ_- polarization, respectively. ρ is basically independent of N in the 3R-stacking, whereas ρ rapidly decreases with N in the 2H-stacking. This result unambiguously proves that the valley information of the exciton formed by the K- (K'-) point states is robustly preserved in the 3R-stacking, in marked contrast to the 2H-stacking. In Fig. 5c, we plot the same data as a function of inverse layer number ($1/N$), and found that the data falls on a straight line, proving us with an opportunity of simple modelling of a relaxation mechanism of valley excitation in multilayer structures.

While the whole difference between the 3R and 2H plots is obvious, one would also notice that the layer-number dependence of ρ in the 2H-stacking is rather unexpected: Since the bilayer and quadralayer flakes are inversion symmetric, ρ of these systems should be negligibly small. In reality, such a large ρ in inversion symmetric bilayer TMDCs has been widely observed[11,26]. A layer-localized exciton, which is localized in each layer of bilayer rather than spread over two layer, has been proposed to explain this phenomenon[27,45]. This situation is rationalized, taking account of the fact that the substrate surface adds a symmetry-breaking electrostatic potential to the system[26].

Ref. 26 allows us to estimate the potential difference between the neighbouring layers of at least several tens of meV, which is comparable to the first-principles interlayer hopping $t_\perp$[45]. In such a case, hybridization between layers is less effective and excitons tend to be localized at each monolayer. When a circular polarized light generates excitons, those in $\overline{K}$ - ($\overline{K}'$-) point are localized in the upper (lower) layer, and the reduction of ρ is dominated by intralayer/intervalley hopping and interlayer/intravalley hopping (the probability of interlayer/intervalley hopping should be negligible compared to these two hopping). Note that this model should be applied also to 3R-stacking.

Figure 5d displays schematics of the band structures and two relaxation paths, originating from intralayer/intervalley hopping (yellow arrow) and interlayer/intravalley hopping (solid and dotted blue arrows), of *K*-point excitations in bilayer structures of 2H- (left) and 3R- (right) stacking. We here ignored the exciton relaxation paths intrinsic to indirect-gap nature of the systems, as it is irrelevant to the PL polarization observed in the present energy region. Inside each layer, the intervalley hopping between *K*- and *K'*-points is the most dominant valley relaxation mechanism for both forms. Another relevant relaxation path is the interlayer/intravalley hopping preserving the momentum of excitons, which is very contrasting between 2H- and 3R-stackings. In the 2H-stacking, this hopping accompanies the reduction of ρ, whereas ρ is not affected in the 3R-stacking (see Fig. 5d). Moreover, from the first-principle calculation, we have found that the interlayer hopping is much suppressed both in the bulk and bilayer 3R-stackings (see Supplementary Information Section 6). This suggests that the valley exciton is robustly protected from the interlayer hopping by the 3R local stacking. Hence, the interlayer/intralayer hopping can be neglected for the 3R-stacking during the discussions on ρ. It is to be pointed out that the above simple view explains the observed behaviour of both 2H- and 3R-stackings (Figs. 5a,b,c).

Here we assume that the number of the intervalley or interlayer hopping paths determines the circular dichroic polarization ρ. Given the number of the interlayer hopping paths for the outermost layer and the inner layers are one and two, respectively, the hopping probability *P* will be

$a\frac{2+2(N-2)}{N}+b$ by simply counting the number of hopping paths per layer. Here, *a* and *b* denotes the interlayer/intravalley and intralayer/intervalley scattering rates, respectively. The observed polarization ρ can be expressed as 1-*P*, and we obtained $\rho = 2a\frac{1}{N}+1-2a-b$. For the 3R-stacking, *a* is effectively zero because of the negligibly small interlayer/intravalley hopping and the independence between this hopping and reduction of ρ as discussed above. The dashed lines in Figs. 5b,c are the least square fit, showing fair agreement with the experimental points. The fitting parameter were a_{2H}=0.28, b_{2H}=0.44, and b_{3R}=0.43, respectively. Within this model, the interlayer relaxation rate is of the same order as the intralayer relaxation rate in the 2H-stacking, implying that the important role of the interlayer relaxation in the 2H-form. Note that the *b* value should be dependent on the environment such as substrate or impurities included in the crystal, being suggestive of strong sample dependences.

The *N* independent polarization shown in Fig. 5 provided solid evidence that the local stacking pattern in the 3R-multilayers takes an important role. The high ability of keeping valley information in the 3R-stacking compared to the 2H-stacking should be of significant interest and importance for understanding the nature of valley system and its further developments. The feature 3R-MoS_2 will broaden the opportunities of physical measurements as well as easy fabrication processes for valley-tronic devices.

Conclusion.

To summarize, we have succeeded in observation of spin/valley polarization using a 3R-stacking of MoS_2 crystals by means of SARPES and PL circular dichroism in combination with first principle band calculations. The origin of the experimentally and computationally observed spin polarization in 3R-MoS_2 and its absence in 2H-MoS_2 and WSe_2 is identical to that expected in monolayer MoS_2 and other TMDC families. Furthermore, the noncentrosymmetric 3R-stacking is

extremely useful for preserving the valley information and pushes forward valley/spin-tronics based on 2D crystals.

Methods

Crystal growth.

2H-MoS_2, 2H-WSe_2, and 3R-MoS_2 single crystals were grown by Chemical Vapour Transport (CVT) technique[29]. For 2H-MoS_2 and 2H-WSe_2, we used Iodine as a transport agent. A mixture of Mo, S, and I_2 (for MoS_2) or W, Se, and I_2 (for WSe_2) was sealed in a quartz tube and was placed in a two-zone horizontal temperature gradient furnace: the higher temperature side (T_H) was kept at 900 ℃ for 14 days while lower side (T_L) was 700 ℃. For 3R-MoS_2, as a transport agent, we used chlorine which was introduced as $MoCl_5$. T_H was kept at 1100 ℃ for 3 days while T_L was 900 ℃. 3R-MoS_2 crystals and multilayers are stable at room temperature, once they are fabricated.

Convergent-beam electron diffraction (CBED) experiments

To confirm the crystal structure of 2H- and 3R-MoS_2, we conducted convergent-beam electron diffraction (CBED) experiments. Thin foil specimens for the CBED experiment were prepared by crushing single crystals. CBED patterns were obtained using JEM-2100F at an accelerating voltage of 200 kV. Figure 2b in the main Letter shows CBED patterns of 2H- and 3R-MoS_2 with [0001] incidence at room temperature.

References

1. Radisavljevic, B., Radenovic, A., Brivio, J., Giacometti, V. & Kis, A. Single-layer MoS_2 transistors. *Nature Nanotech.* **6**, 147-150 (2011).

2. Podzorov, V., Gershenson, M. E., Kloc, Ch., Zeis, R. & Bucher, E. High-mobility field-effect transistors based on transition metal dichalcogenides. *Appl. Phys. Lett.* **84**, 3301 (2004).

3. Zhang, Y. J., Ye, J. T., Matsuhashi, Y. & Iwasa, Y. Ambipolar MoS_2 Thin flake transistors. *Nano Lett.* **12**, 1136-1140 (2012).

4. Braga, D., Lezama, I. G., Berger, H. & Morpurgo, A. F. Quantitative determination of the band gap of WS_2 with ambipolar ionic liquid-gated transistors. *Nano Lett.* **12**, 5218-5223 (2012).

5. Ye, J. T., Zhang, Y. J., Akashi, R., Bahramy, M. S., Arita, R. & Iwasa, Y. Superconducting dome in a gate-tuned band insulator. *Science* **338**, 1193-1196 (2012).

6. Taniguchi, K., Matsumoto, A., Shimotani, H. & Takagi, H. Electric-field-induced superconductivity at 9.4K in a layered transition metal disulphide MoS_2. *Appl. Phys. Lett.* **101**, 042603 (2012).

7. Yuan, H. T., Bahramy, M. S., Morimoto, K., Wu, S., Nomura, K., Yang, B. J., Shimotani, H., Suzuki, R., Toh, M. L., Kloc, C., Xu, X., Arita, R., Nagaosa, N & Iwasa, Y. Zeeman-type spin splitting controlled by an electric field. *Nature Phys.* **9**, 563-569 (2013).

8. Mak, K. F., Lee, C., Hone, J., Shan, J. & Heinz, T. F. Atomically thin MoS_2: A new direct-gap semiconductor. *Phys. Rev. Lett.* **105**, 136805 (2010).

9. Splendiani, A., Sun, L., Zhang, Y., Li, T., Kim, J., Chim, C., Galli, G. & Wang F. Emerging photoluminescence in monolayer MoS_2. *Nano Lett.* **10**, 1271-1275 (2010).

10. Zeng, H., Dai, J., Yao, W., Xiao, D. & Cui, X. Valley polarization in MoS_2 monolayers by optical pumping. *Nature Nanotech.* **7**, 490-493 (2012).

11. Mak, K. F., He, K., Shan, J. & Heinz, T. F. Control of valley polarization in monolayer MoS_2 by optical helicity. *Nature Nanotech.* **7**, 494-498 (2012).

12. Sallen, G., Bouet, L., Marie, X., Wang, G., Zhu, C. R., Han, W. P., Lu, Y., Tan, P. H., Amand, T., Liu, B. L. & Urbaszek B. Robust optical emission polarization in MoS_2 monolayers through selective valley excitation. *Phys. Rev. B* **86**, 081301 (2012).

13. Cao, T., Wang, G., Han, W., Ye, H., Zhu, C., Shi, J., Niu, Q., Tan, P., Wang, E., Liu, B. & Feng, J. Valley-selective circular dichroism of monolayer molybdenum disulphide. *Nat. Commun.* **3**, 887

(2012).

14. Takashina, K., Ono, Y., Fujiwara, A., Takahashi, Y. & Hirayama, Y. Valley polarization in Si(100) at zero magnetic field. *Phys. Rev. Lett.* **96**, 236801 (2006).

15. Isberg, J., Gabrysch, M., Hammersberg, J., Majdi, S., Kovi, K. K. & Twitchen, D. J. Generation, transport and detection of valley-polarized electrons in diamond. *Nature Mater.* **12**, 760-764 (2013).

16. Shkolnikov, Y. P., De Poortere, E. P., Tutuc, E. & Shayegan, M. Valley splitting of AlAs two-dimensional electrons in a perpendicular magnetic field. *Phys. Rev. Lett.* **89**, 226805 (2002).

17. Gunawan, O. et al. Valley susceptibility of an interacting two-dimensional electron system. *Phys. Rev. Lett.* **97**, 186404 (2006).

18. Gunawan, O., Gokmen, T., Vakili, K., Padmanabhan, M., De Poortere, E. P. & Shayegan, M. Spin-valley phase diagram of the two-dimensional metal-insulator transition. *Nature Phys.* **3**, 388-391 (2007).

19. Zhu, Z., Collaudin, A., Fauque, B., Kang, W. & Behnia K. Field-induced polarization of Dirac valleys in bismuth. *Nature Phys.* **8**, 89-94 (2012).

20. Xiao, D., Yao, W. & Niu, Q. Valley-Contrasting Physics in Graphene: Magnetic moment and topological transport. *Phys. Rev. Lett.* **99**, 236809 (2007).

21. Rycerz, A., Tworzydlo, J. & Beenakker, C. W. J. Valley filter and valley valve in graphene. *Nature Phys.* **3**, 172–175 (2007).

22. Yao, W., Xiao, D. & Niu, Q. Valley-dependent optoelectronics from inversion symmetry breaking. *Phys. Rev. B*, **77**, 235406 (2008).

23. Gunlycke, D. & White, C. T. Graphene valley filter using a line defect. *Phys. Rev.Lett.* **106**, 136806 (2011).

24. Xiao, D., Liu, G., Feng, W., Xu, X. & Yao, W. Coupled spin and valley physics in monolayers of MoS_2 and other group-VI dichalcogenides. *Phys. Rev. Lett.*, **108**, 196802 (2012).

25. Zhu, C. R., Wang, G., Liu, B. L., Marie, X., Qiao, X. F., Zhang, X., Wu, X. X., Fan, H., Tan, P. H., Amand, T. & Urbaszek, B. Strain tuning of optical emission energy and polarization in monolayer and bilayer MoS_2. *Phys. Rev. B* **88**, 121301 (2013).

26. Wu, S., Ross, J. S., Liu, G. B., Aivazian, G., Jones, A., Fei, Z., Zhu, W., Xiao, D., Yao, W., Cobden, D. & Xu, X. Electrical tuning of valley magnetic moment through symmetry control in bilayer MoS_2. *Nature Phys.* **9**, 149-153 (2013).

27. Jones, A. M., Yu, H., Ross, J. S, Klement, P., Ghimire, N. J., Yan, J., Mandrus, D. G., Yao, W. & Xu, X. Spin-layer locking effects in optical orientation of exciton spin in bilayer WSe_2. *Nature Phys.* **10**, 130-134 (2014).

28. Wilson, J. A. & Yoffe, A. D. The transition metal dichalcogenides discussion and interpretation of the observed optical, electrical and structural properties. *Adv. Phys.* **18**, 193-334 (1969).

29. Wildervanck, J. C. *Doctoral dissertation, Groningen* (1970).

30. Zhu, Z. Y., Cheng, Y. C. & Schwingenschlogl, U. Giant spin-orbit-induced spin splitting in two-dimensional transition-metal dichalcogenide semiconductors. *Phys. Rev. B* **84**, 153402 (2011).

31. Lee, Y., Zhang, X., Zhang, W., Chang, M., Lin, C., Chang, K., Yu, Y., Wang, J. T., Chang, C., Li, L. & Lin, T. Synthesis of large-area MoS_2 atomic layers with chemical vapor deposition. *Adv. Mater.* **24**, 2320-2325 (2012).

32. Wu, S., Huang, C., Aivazian, G., Ross, J. S., Cobden, D. H. & Xu, X. Vapor-solid growth of high optical quality MoS_2 monolayers with near-unity valley polarization. *ACS Nano* **7**, 2768-2772 (2013).

33. Liu, K-K. et al. Growth of large-area and highly crystalline MoS_2 thin layers on insulating substrates. *Nano Lett.* **12**, 1538-1544 (2012).

34. Towle, L. C., Oberbeck, V., Brown, B. E. & Stajdohar, R. E. Molybdenum diselenide: rhombohedral high pressure-high temperature polymorph. *Science* **154**, 895-896 (1966).

35. Al-hilli, A. A. & Evans, B. L. The preparation and properties of transition metal dichalcogenide single crystals. *J. Cryst. Grow.* **15**, 93-101 (1972).

36. Beal, A. R., Knights, J. C. & Liang, W. Y. Transmission spectra of some transition metal dichalcogenides. II. Group VIA: Trigonal prismatic coordination. *J. Phys. C: Solid State Phys.* **5**, 3540-3551 (1972).

37. Coehoorn, R., Haas, C., Dijkstra, J., Flipse C. J. F., de Groot, R. A. & Wold, A. Electronic structure of $MoSe_2$, MoS_2, and WSe_2. I. Band-structure calculations and photoelectron spectroscopy. *Phys. Rev. B* **35**, 6195–6202 (1987).

38. Jin, W., Yeh, P.-C., Zaki, N., Zhang, D., Sadowski, J. T., Al-Mahboob, A., van der Zande, A. M., Chenet, D. A., Dadap, J. I., Herman, I. P., Sutter, P., Hone, J. & Osgood, R. M. Jr. Direct measurement of the thickness-dependent electronic band structure of MoS_2 using angle-resolved photoemission spectroscopy. *Phys. Rev. Lett.* **111**, 106801 (2013).

39. Ishizaka, K., Bahramy, M. S., Murakawa, H., Sakano, M., Shimojima, T., Sonobe, T., Koizumi, K., Shin, S., Miyahara, H., Kimura, A., Miyamoto, K., Okuda, T., Namatame, H., Taniguchi, M., Arita, R., Nagaosa, N., Kobayashi, K., Murakami, Y., Kumai, R., Kaneko, Y., Onose, Y. & Tokura, Y. Giant Rashba-type spin splitting in bulk BiTeI. *Nature Mater.* **10**, 521-526 (2011).

40. Okuda, T., Miyamoto, K., Miyahara, H., Kuroda, K., Kimura, A., Namatame, H. & Taniguchi, M. Efficient spin resolved spectroscopy observation machine at Hiroshima Synchrotron Radiation Center. *Rev. Sci. Instrum.* **82**, 103302 (2011).

41. Meier, F., Dil, H., Lobo-Checa, J., Patthey, L. & Osterwalder, J. Quantitative vectorial spin analysis in angle-resolved photoemission: Bi/Ag(111) and Pb/Ag(111). *Phys. Rev. B* **77**, 165431 (2008)

42. Sakamoto, K., Kim, T. H., Kuzumaki, T., Müller, B., Yamamoto, Y., Ohtaka, M., Osiecki, J. R., Miyamoto, K., Takeichi, Y., Harasawa, A., Stolwijk, S. D., Schmidt, A. B., Fujii, J., Uhrberg, R. I. G., Donath, M., Yeom, H. W. & Oda T. Valley spin polarization by using the extraordinary Rashba effect on silicon. *Nat. Commun.* **4**, 2073 (2013).

43. Lee, C., Yan, H., Brus, L. E., Heinz, T. F., Hone, J. & Ryu, S. Anomalous lattice vibrations of single- and few-layer MoS_2. *ACS Nano* **4**, 2695-2700 (2010).

44. Li, H., Zhang, Q., Yap, C. C. R., Tay, B. K., Edwin, T. H. T., Olivier, A. & Baillargeat, D. From bulk to monolayer MoS_2: evolution of Raman scattering. *Adv. Funct. Mater.* **22**, 1385-1390 (2012).

45. Gong, Z., Liu, G. B., Yu, H., Xiao, D., Cui, X., Xu, X. & Yao, W. Magnetoelectric effects and valley-controlled spin quantum gates in transition metal dichalcogenide bilayers. *Nat. Commun.* **4**, 2053 (2013).

Acknowledgements

We thank J. T. Ye, Y. Kasahara, J. Fujioka, S. Z. Bisri and Y. Kaneko for their help in sample preparations and characterizations, T. Shimojima, K. Shirai, and K. Sumida for their help in SARPES measurements, S. Shin, A. Kimura, H. Namatame, M. Taniguchi for sharing SARPES infrastructure, and Y. Nomura for useful comments on band structure calculations. T. Banno for his help in maintenance of PL measurement system. R.S. is supported by Leading Graduate Program of Materials Education program for the future leaders in Research, Industry, and Technology (MERIT). M.S. and Y.J.Z. are supported by Advanced Leading Graduate Course for Photon Science (ALPS) and by a research fellowship for young scientists from JSPS. This research was partly supported by the Strategic International Collaborative Research Program (SICORP-LEMSUPER) and Precursory Research for Embryonic Science and Technology (PRESTO), Japan Science and Technology Agency, Research Hub for Advanced Nano Characterization, The University of Tokyo, supported by MEXT, Japan, as well as by Grant-in-Aid for Scientific for Specially Promoted Research (No. 25000003, No.23244066) and the `Funding Program for World-Leading Innovative R&D on Science and Technology (FIRST Program)' from JSPS, Japan.

Author contributions

R.S. and M.S. contributed equally to this work. R.S., Y.Z. Y.I. conceived and designed the research. R.S. grew and characterized all the crystals used in this research, and D.M. took CBED patterns. M.S., K.I., A.H., K.Y., K.K., K.M., T.O. performed SARPES measurements. M.S., K.I. analysed (S)ARPES data. First principles calculations were made by R.A. and R.A. Y.Z. built a PL measurement system, and R.S. measured the PL spectra. R.S., M.S., Y. Z., R.A., D.M., K.I., R.A., Y.I. wrote the manuscript.

Additional information

Supplementary information accompanies this paper at www.nature.com/naturenanotechnology. Reprints and permission information is available online at http://npg.nature.com/reprintsandpermissions/. Correspondence and requests for materials should be addressed to Y.I. and K. I.

Competing financial interests

The authors declare no competing financial interests.

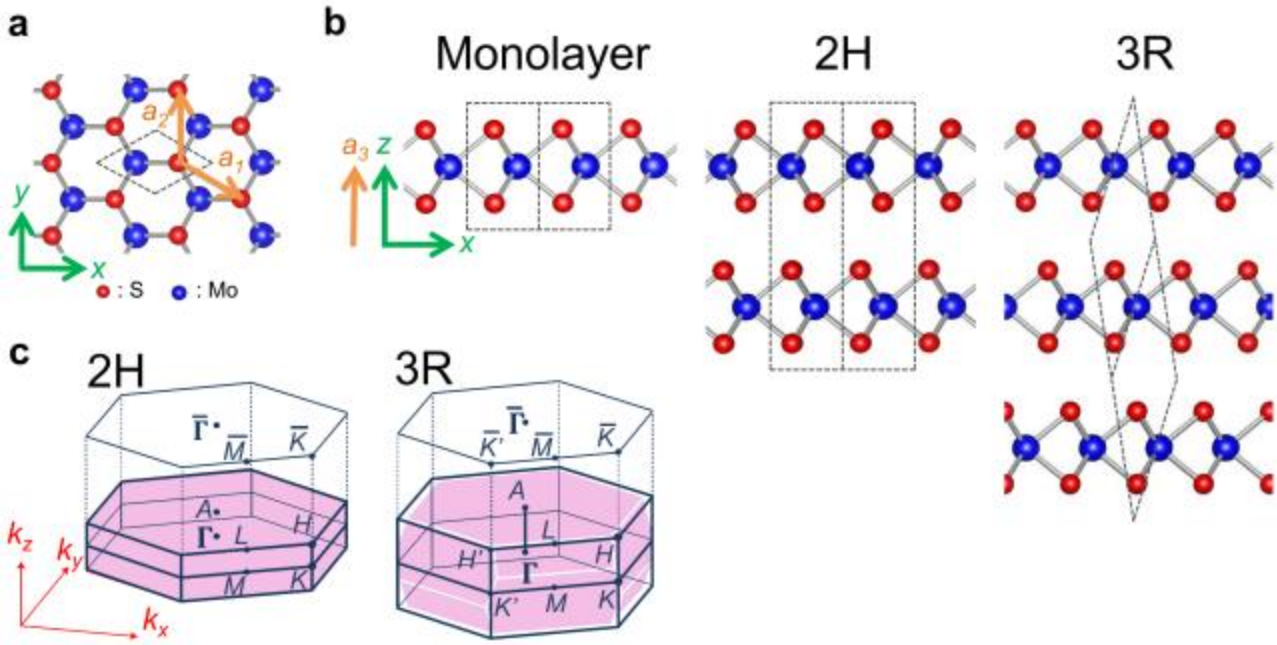

Figure 1 | Crystal structure and Brillouin zones of monolayer, 2H- and 3R-forms of MoS_2.
a, Stick and ball crystal structure of MoS_2 monolayer (top view). **b,** Side views of three forms of MoS_2: (from left to right) monolayer, 2H-crystal, and 3R-crystal. Blue and red spheres correspond to molybdenum and sulphur atoms. Black dashed lines indicate unit cells; orange arrows indicate lattice vectors, whereas green vectors indicate orthogonal axis of the real space. **c,** The first Brillouin zones of 2H- and 3R-MoS_2. The solid blue lines and pink shaded areas represent the conventional and primitive Brillouin Zones, respectively. The hexagonal plane with $\bar{\Gamma}$, $\overline{M}$, $\overline{K}$, and $\overline{K}'$ represents the corresponding two-dimensional projected Brillouin zone.

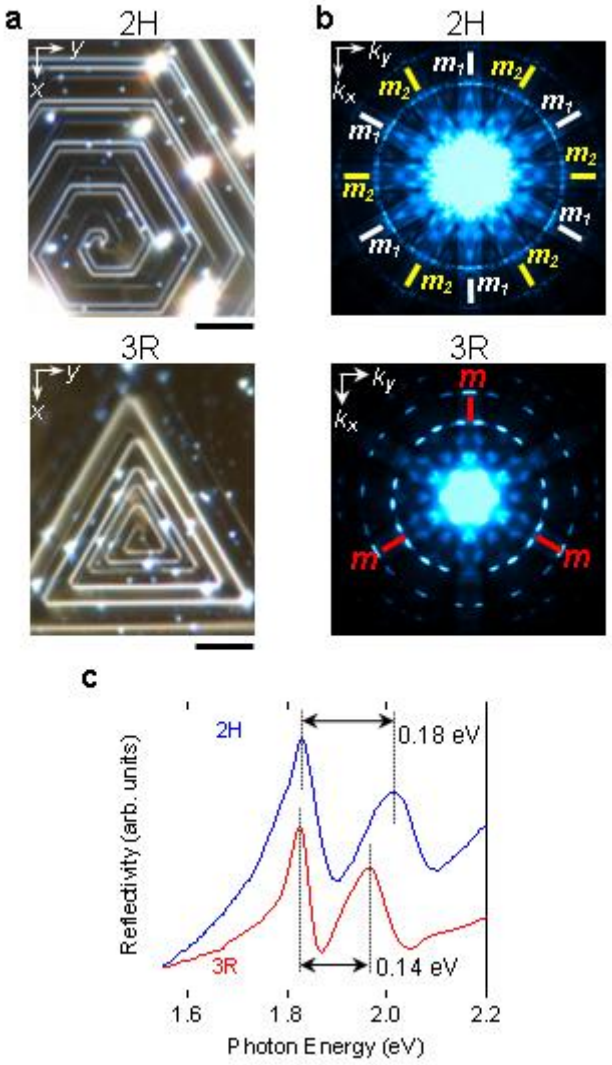

Figure 2 | Structural and optical characterizations of 2H- and 3R- single crystals of MoS_2

a, Optical micrograph image of the surface of MoS_2 crystals showing contrasting screw dislocations reflecting the crystal symmetry. The black scale bars indicate 10 μm. **b,** CBED patterns of MoS_2. The 2H- and 3R-crystals show mirror symmetries, indicated by yellow, white and red lines, at the position of the 6-fold and 3-fold symmetry, respectively. **c,** Optical reflectivity spectra for 2H- and 3R- crystals. The two-peak structures are assigned as exciton transitions. The energy splitting was 0.18 eV and 0.14 eV, for 2H- and 3R- crystals, respectively, being consistent with previous literature[28,36].

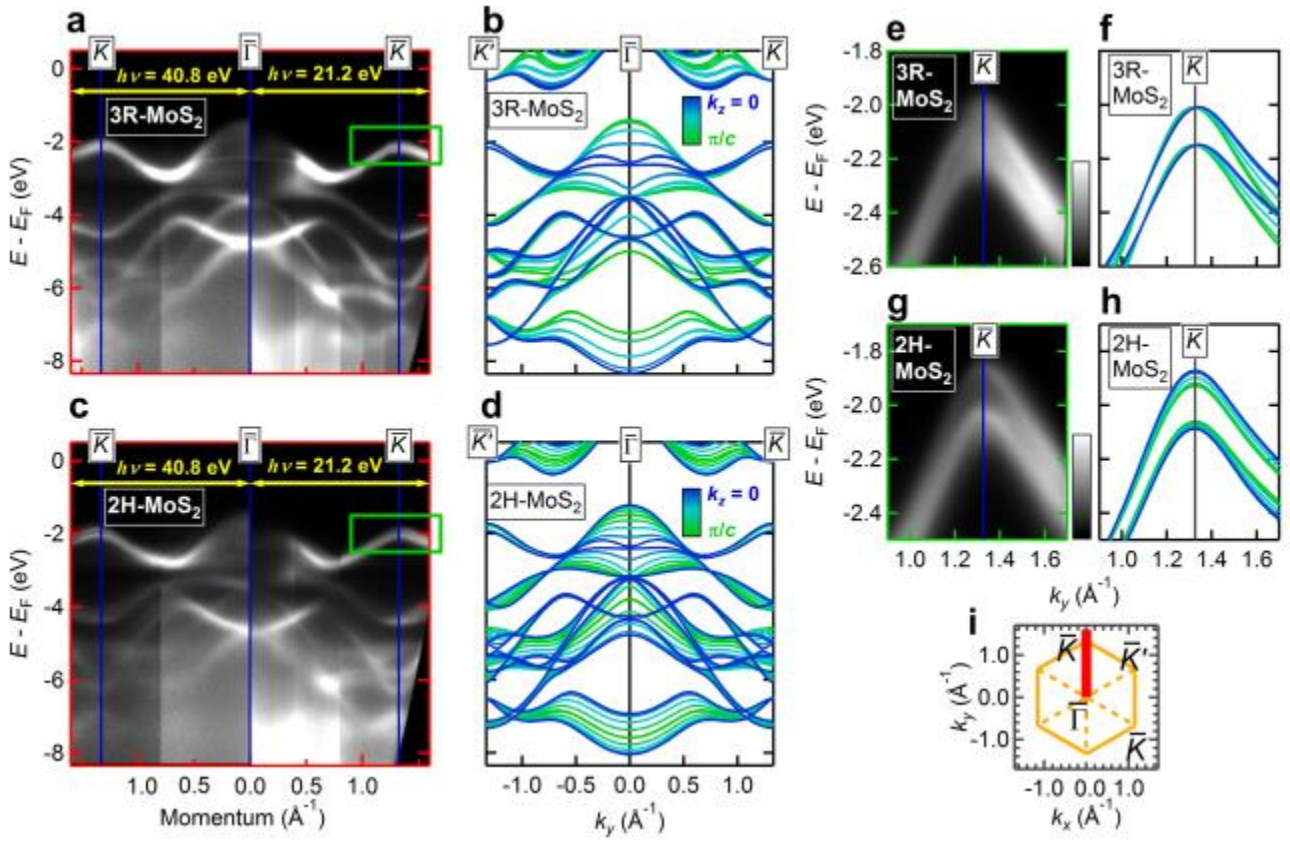

Figure 3 | Valence band structures of 3R- and 2H-MoS_2

a, Valence band structures of 3R-MoS_2 recorded along $\overline{\Gamma}-\overline{K}$ shown as the red line in **i**) by ARPES using $h\nu$ = 40.8 eV (left) and 21.2 eV (right), respectively. **b,** Bulk band structures of 3R-MoS_2 along k_y obtained by the first principles calculations. The band dispersions for various k_z, indicated by the inset colour-scale, are overlapped. **c,d,** Band structures of 2H-MoS_2 obtained by ARPES and calculation in the similar manner. **e,f,** The ARPES image and the corresponding calculation focusing near the valence band top at $\overline{K}$–point for 3R-MoS_2. **g,h,** ARPES image and calculation for 2H-MoS_2. The region of measurements for **e** and **g** corresponds to the green rectangles in panels **a** and **c**, respectively. **i,** Momentum cut of the measurement region in **a** depicted as the red line, overlaid on the projected two-dimensional first Brillouin zone of 3R-MoS_2.

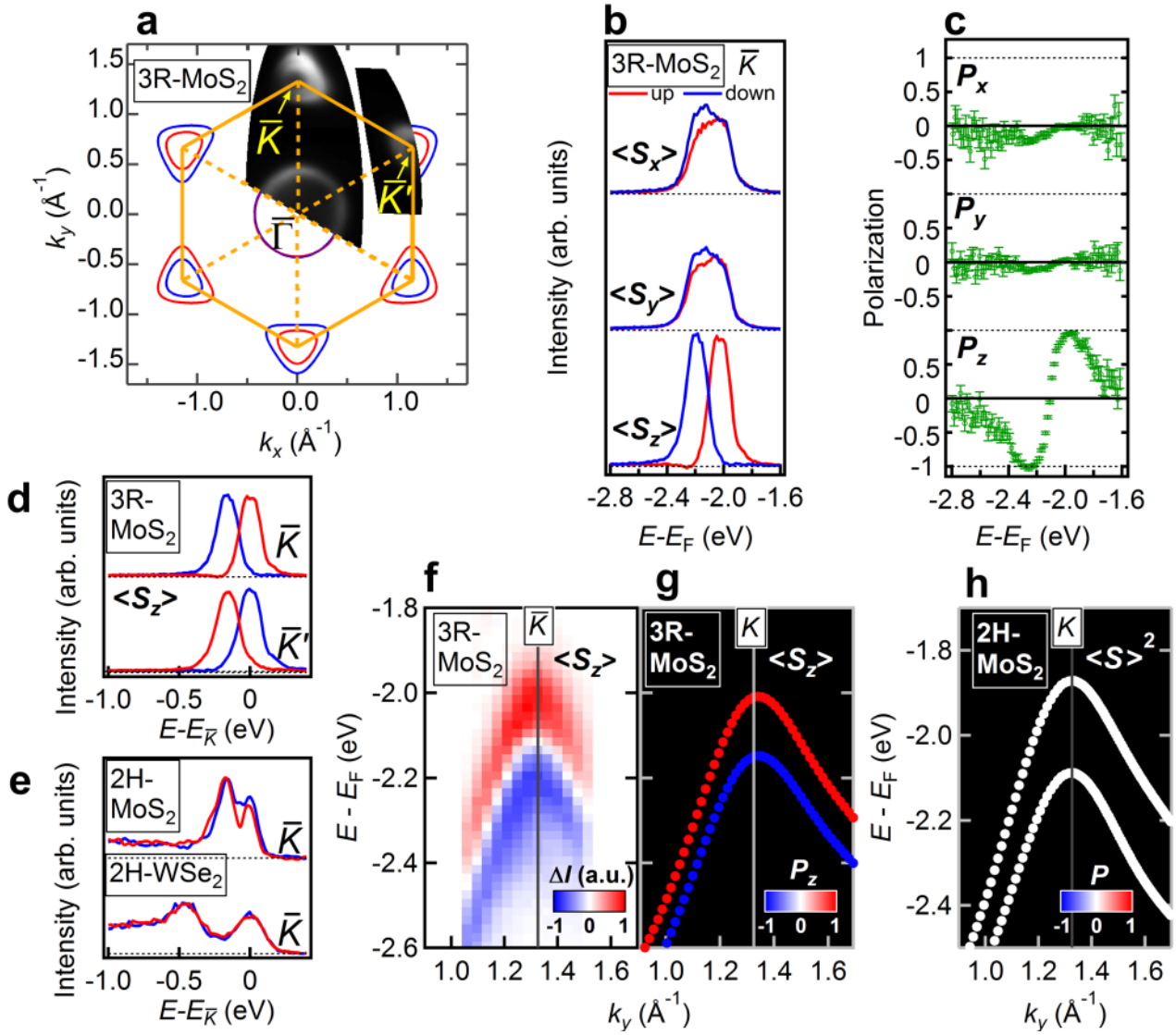

Figure 4 |Detection of the spin polarization near the valence band top at $\overline{K}$– and $\overline{K'}$- point.

a, Intensity mapping at 0.3 eV relative to the top of the valence band at $\overline{K}$-point ($E - E_{\overline{K}} = -0.3$ eV) obtained by ARPES ($h\nu$ = 21.2 eV) and the calculated equi-energy surfaces at $k_z = \pi/c$ overlaid on the 2D first Brillouin zone. Hereafter in this Figure, the red (blue) colour indicates spin-up (-down) component. **b,c,** Spin-resolved energy distribution curves (EDCs) at $\overline{K}$-point and the corresponding spin-polarization with error-bars for 3R-MoS_2 obtained by SARPES. Here, the quantization axes of spin are along the *x*, *y, z* crystal axes defined in Fig. 1a (see SI for detailed analysis). **d,** Spin-resolved EDCs for spin along *z*-axis, recorded at the inequivalent valleys of $\overline{K}$- and $\overline{K}$'-points. **e,** Spin-resolved EDCs at $\overline{K}$-point from the centrosymmetric materials 2H-MoS_2 and 2H-WSe_2 (see SI for detailed analysis). **f,** The image obtained by the subtraction of the SARPES intensities for *z*-oriented spin-up and -down (ΔI) recorded along k_y. **g** Calculated spin polarizations P_z of the valence bands along (0, k_y ,0) for 3R-MoS_2. **h,** Calculated total spin polarization of the valence bands along (0, k_y ,0) for centrosymmetric 2H-MoS_2.

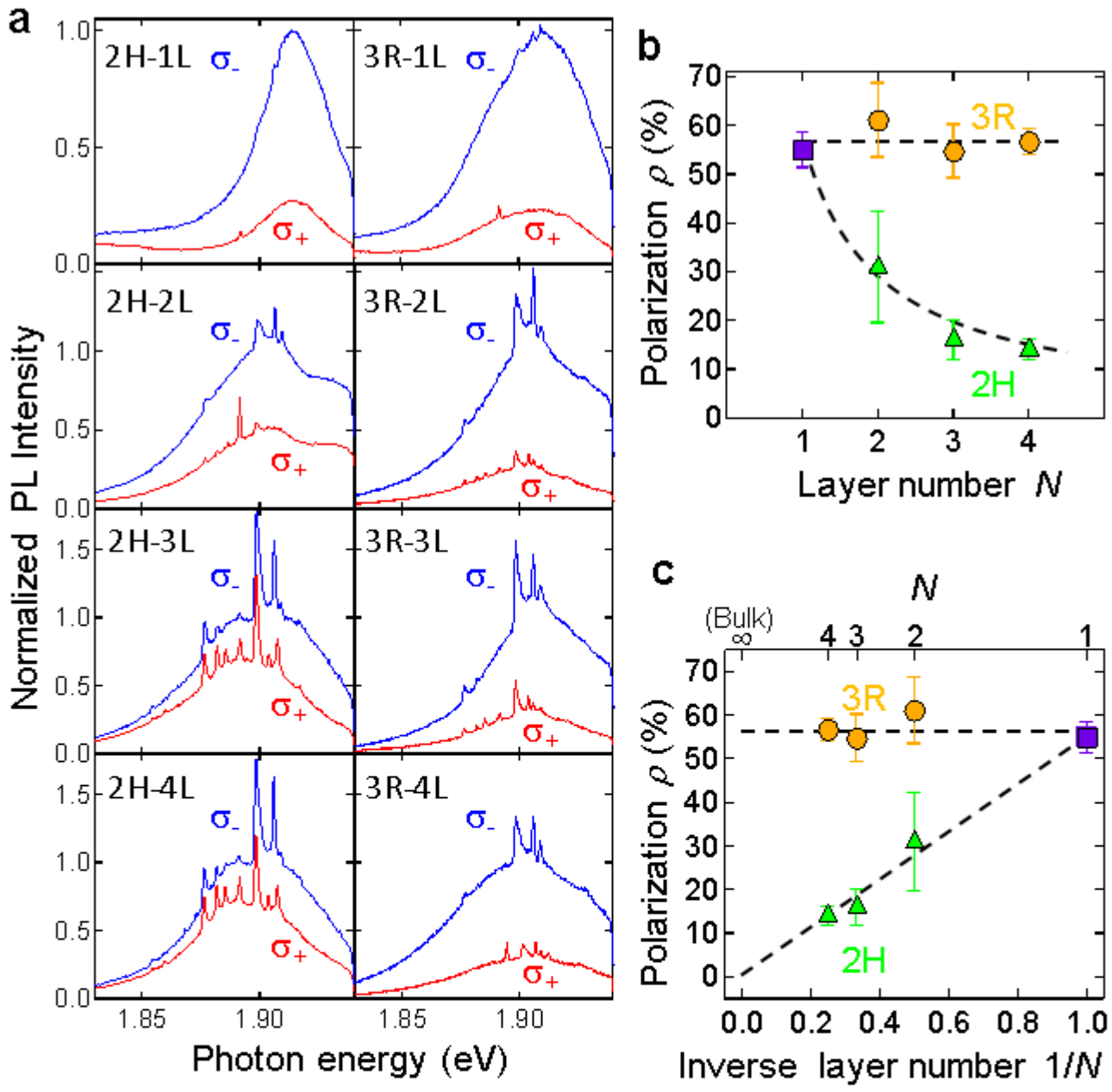
a
2H-1L
3R-1L
2H-2L
3R-2L
2H-3L
3R-3L
2H-4L
3R-4L
σ-
σ+
Normalized PL Intensity
Photon energy (eV)
b
Polarization ρ (%)
3R
2H
Layer number N
c
N
(Bulk)
∞
Polarization ρ (%)
Inverse layer number 1/N
d
2H
3R
K
K'
Upper layer
Lower layer

Figure 5 | Circular dichroic photoluminescence of bilayer 2H- and 3R-MoS_2

a, Circularly polarized PL spectra at 4 K for mono-, bi-, tri-, and quadra-layers of 2H- (left column) and 3R- (right column) MoS_2, pumped by a left circularly polarized (σ_-) He-Ne laser with a 633 nm wavelength. Sharp structures are Raman peaks from MoS_2 and Si substrate. **b,** Layer number dependence of polarization ρ for 2H- and 3R-stackings with error-bars. **c,** Inverse layer number dependence of polarization ρ for 2H- and 3R-stackings with error-bars. Dashed lines in **b** and **c** are the least square fit by the model described in the text. **d,** Schematic crystal and band structures of 2H- and 3R-bilayer MoS_2. The valence bands coloured with red and blue correspond to the spin-up and -down states, respectively. The green conduction bands are not spin-polarized. The character of the valence bands are exchanged between *K*- and *K'*- points in the 2H-stacking, while that is preserved in the 3R. The white and black spheres indicate holes and electrons forming excitons at the *K*-point by illumination of circularly polarized light. Intralayer relaxation shown by yellow arrows is the intervalley scattering from *K*- to *K'*-point. In the 2H-stacking, the interlayer scattering indicated by a blue arrow is also an effective relaxation mechanism for multilayer 2H-stacking. In the 3R-stacking, on the other hand, the interlayer scattering indicated by a blue dotted line is much suppressed, and it does not reduce the polarization ρ.